RSC Advances

PAPER

View Article Online
View Journal | View Issue

Cite this: *RSC Adv.*, 2021, **11**, 29576

Electronic and optical properties of two-dimensional heterostructures based on Janus XSSe (X = Mo, W) and $Mg(OH)_2$: a first principles investigation

Junbin Lou,[a] Kai Ren,*[b] Zhaoming Huang,*[c] Wenyi Huo,[b] Zhengyang Zhu[c] and Jin Yu[d]

Received 19th July 2021
Accepted 19th August 2021

DOI: 10.1039/d1ra05521f

rsc.li/rsc-advances

Two-dimensional (2D) materials have attracted numerous investigations after the discovery of graphene. 2D van der Waals (vdW) heterostructures are a new generation of layered materials, which can provide more desirable applications. In this study, the first principles calculation was implemented to study the heterostructures based on Janus TMDs (MoSSe and WSSe) and $Mg(OH)_2$ monolayers, which were constructed by vdW interactions. Both $MoSSe/Mg(OH)_2$ and $WSSe/Mg(OH)_2$ vdW heterostructures have thermal and dynamic stability. Besides, $XSSe/Mg(OH)_2$ (X = Mo, W) possesses a direct bandgap with a type-I band alignment, which provides promising applications for light-emitting devices. The charge density difference was investigated, and 0.003 (or 0.0042) |e| were transferred from MoSSe (or WSSe) layer to $Mg(OH)_2$ layer, and the potential drops were calculated to be 11.59 and 11.44 eV across the interface of the $MoSSe/Mg(OH)_2$ and $WSSe/Mg(OH)_2$ vdW heterostructures, respectively. Furthermore, the $MoSSe/Mg(OH)_2$ and $WSSe/Mg(OH)_2$ vdW heterostructures have excellent optical absorption wave. Our studies exhibit an effective method to construct new heterostructures based on Janus TMDs and develop their applications for future light emitting devices.

1. Introduction

Nowadays, two-dimensional (2D) materials have attracted numerous investigations since graphene was prepared by a mechanical stripping method.[1] Graphene was discovered to have novel thermal and electronic properties resulting from the linear band structure near the Dirac cone with zero bandgap.[2–9] However, these characteristics of graphene also limit the applications in some nano-devices, which ueged the studies on 2D semiconductors.[10–17] Transition metal dichalcogenide (TMD) materials are one of the common layered semiconductor materials, which have excellent electronic,[18] thermal,[19] and optical properties.[20,21] For example, the n-doping of WSe_2 was performed by the chemical vapor deposition (CVD) method, which can be used as an air-stable n-MOSFET possessing a mobility of about 70 $cm^2\ V^{-1}\ s^{-1}$.[22] MoS_2 has high interfacial thermal conductance, about 2.0×10^8 $W\ K^{-1}\ m^{-2}$ with Au by different interfacial angles, and the thermal ability of TMDs can also be decided by layers.[23] Similar to graphene nanoribbons, the mobility of the MoS_2 monolayer is 200 $cm^2\ V^{-1}\ s^{-1}$ at room temperature, indicating promising applications in tunnel FETs and transistors.[24] TMD materials are also reported to act as substrates to prepare 2D germanene[25] or nitrogen-doped graphene, which are efficient catalysts for redox reactions.[26] All these excellent properties of 2D materials show the promising applications for further nano-devices.[27–31]

In order to expand the application of these layered materials, more interesting properties were developed by the prediction of 2D materials.[32–36] For example, δ-phosphorene was proposed to be an auxetic material with a high negative Poisson's ratio (NPR) of about −0.267 along relative direction.[37] FeB_2 monolayer possesses a Dirac cone, which endows it with a Fermi velocity larger than that of graphene.[38] Using first principles calculations, 2D TiC_3 was reported by a remarkably novel storage capacity of about 1278 mA h g^{-1} even with low barrier energy.[39] The new generation of 2D materials are promising candidates for the usages of photocatalytic, photovoltaic, and optical devices.[40] Besides, constructing a heterostructure by two different layered materials is also a decent method to create more applications for 2D materials.[41–43] The novel electronic,[44] interfacial[45] and optical[29] properties of heterostructures formed by van der Waals (vdW) interactions have been exploited for

[a]School of Information Science and Engineering, Jiaxing University, Jiaxing, Zhejiang, China
[b]School of Mechanical and Electronic Engineering, Nanjing Forestry University, Nanjing, Jiangsu, China. E-mail: kairen@njfu.edu.cn
[c]School of Mechanical Engineering, Wanjiang University of Technology, Maanshan, Anhui, China
[d]School of Materials Science and Engineering, Southeast University, Nanjing, Jiangsu, China

catalysis,[46,47] electronics and optoelectronics.[48] C_2N/WS_2 vdW possesses a high carrier mobility of 2406.50 $cm^2 V^{-1} s^{-1}$ for holes along some transportation directions.[49] BCN/C_2N vdW can be used as a direct Z-Scheme photocatalyst for water splitting with the e–h recombination time of about 2 ps.[50] Recently, black/red phosphorus was investigated to possess type-I band alignment and also could switch to a Z-scheme photocatalyst.[51] A type-I heterostructure, $MoTe_2/WSe_2$, showed a novel photoluminescence performance from the $MoTe_2$ layer (about 1.1 eV).[52] The PbI_2/WS_2 heterostructure also possessed an intrinsic type-I band structure with a decent narrower bandgap; interestingly, the diffusion coefficients of PbI_2 for electrons and holes were similar to about 0.039 and 0.032 $cm^2 s^{-1}$, respectively.[53] All these studies demonstrate the promising applications for future light emitting devices[54] and optoelectronic applications.[55–57] Recently, among tremendous 2D material family, TMDs with the Janus structure have attracted wide attention, which destroy the symmetry of the original crystal structure inducing more novel properties[10,58] after the preparation of MoSSe.[59,60] The Janus TMD materials have pronounced carrier mobility ranging from 28 to 606 $cm^2 V^{-1} s^{-1}$.[61,62] Besides, a Janus chromium dichalcogenide was proved to have the ability to separate the photogenerated electrons and holes, and the excited carriers had a lifetime of about 2 ns calculated by the time domain density functional theory.[63] Interestingly, the electronic property of the MoSSe monolayer can be tuned by a tensile strain from direct to indirect bandgap, and the excellent visible-light absorption performance promises its use as a photocatalyst.[64] The WSSe monolayer can be used as a promising HER catalyst because the basal plane can be easily activated and such Janus asymmetry can enhance the HER activity.[65] The dipole moment, vibrational frequency, and Rashba parameters of WSSe were also induced by its asymmetric Janus structure,[66] which have potential usage for efficient photocatalysts. More recently, monolayered $Mg(OH)_2$ sheets were reported to be obtained by the hydrothermal crystal growth technique with stable and classy chemical and vibrational properties, which are potential candidates as flexible optoelectronics.[67] 2D $Mg(OH)_2$ also showed unique structural and electronic characteristics in the heterostructure.[68,69] Moreover, some MoSSe- and WSSe-based heterostructures have been reported, such as MoSSe/WSSe,[70] Hf_2NT_2/MSSe (T = F, O, OH; M = Mo, W),[71] MoSSe/WSe_2,[72] graphene/MoSSe,[73] while reports on MoSSe/$Mg(OH)_2$ and WSSe/$Mg(OH)_2$ heterostructures are still rare. Therefore, considering such novel electronic and optical properties of such synthesized MoSSe, WSSe and $Mg(OH)_2$, it is worth constructing the heterostructures by XSSe (X = Mo, W) and $Mg(OH)_2$ to develop the charming characteristics and the potential applications.

Therefore, in this study, we performed the first principles calculation, to investigate the heterostructures formed by Janus TMDs (MoSSe and WSSe) and $Mg(OH)_2$. After deciding the structure of the heterostructures, the thermal and dynamic stabilities were addressed. Then, the band alignment of those layered materials was checked, and the interfacial characteristics, charge density difference and potential drop were studied. The optical properties were also calculated from the optical absorption spectrum.

2. Methods

Based on the density functional theory (DFT), in this simulation work, the first principles calculation was employed, which was implemented by the Vienna *ab initio* simulation package (VASP).[74] We used the projector augmented wave potentials (PAW) and generalized gradient approximation (GGA) to explain the core electron and exchange correlation functional, respectively,[75–77] using the Perdew–Burke–Ernzerhof (PBE) functional. To achieve more accurate results of the bandgap, the Heyd–Scuseria–Ernzerhof (HSE06; screening parameter 0.2 $Å^{-1}$, mixing parameter 0.25) exchange–correlation functionals were used.[78] The cut-off energy was set as 550 eV, and the *k*-point grids of the Monkhorste–Pack in the first Brillouin zone was 15 × 15 × 1. Besides, the DFT-D3 method of Grimme was also conducted for the corrections of the vdW and dipole.[79] A thickness of 25 Å was employed for the vacuum layer to prevent the interactions of the layers. The energy of the calculated system and Hellmanne–Feynman force were controlled with a convergence within 1×10^{-5} eV and 0.01 eV·$Å^{-1}$, respectively. For the calculation of the phonon spectra, the density functional perturbation theory (DFPT) within the PHONOPY code was used.[80,81]

The binding energy (E) of the layered materials in this work was calculated by the following equation:

$$E = E_{\mathrm{H}} - E_{\mathrm{XSSe}} - E_{\mathrm{Mg(OH)_2}}, \quad (1)$$

where E_{H}, E_{XSSe} and $E_{\mathrm{Mg(OH)_2}}$ represent the total energy of the XSSe/$Mg(OH)_2$ heterostructure, XSSe and $Mg(OH)_2$ monolayers, respectively. The charge-density difference ($\Delta\rho$) of the XSSe/$Mg(OH)_2$ heterostructure was obtained from the following equation:

$$\Delta\rho = \rho_{\mathrm{H}} - \rho_{\mathrm{XSSe}} - \rho_{\mathrm{Mg(OH)_2}}, \quad (2)$$

where ρ_{H}, ρ_{XSSe} and $\rho_{\mathrm{Mg(OH)_2}}$ are used to explain the charge density of the isolated XSSe/$Mg(OH)_2$ heterostructure, XSSe and $Mg(OH)_2$ monolayers, respectively. The optical absorption of the materials was obtained using the following formula:

$$\alpha(\omega) = \frac{\sqrt{2}\omega}{c}\left\{\left[\varepsilon_1^2(\omega) + \varepsilon_2^2(\omega)\right]^{1/2} - \varepsilon_1(\omega)\right\}^{1/2} \quad (3)$$

where ω, α and c are utilized to express angular frequency, absorption coefficient and the speed of light, respectively, and $\varepsilon_1(\omega)$ and $\varepsilon_2(\omega)$ are the dielectric constant for real and imaginary parts.

3. Results and discussion

The structures of the monolayered MoSSe, WSSe and $Mg(OH)_2$ were optimized first, as shown in Fig. 1. The calculated lattice parameters of MoSSe, WSSe and $Mg(OH)_2$ were 3.228, 3.269 and 3.140 Å, respectively, showing the very small lattice mismatch

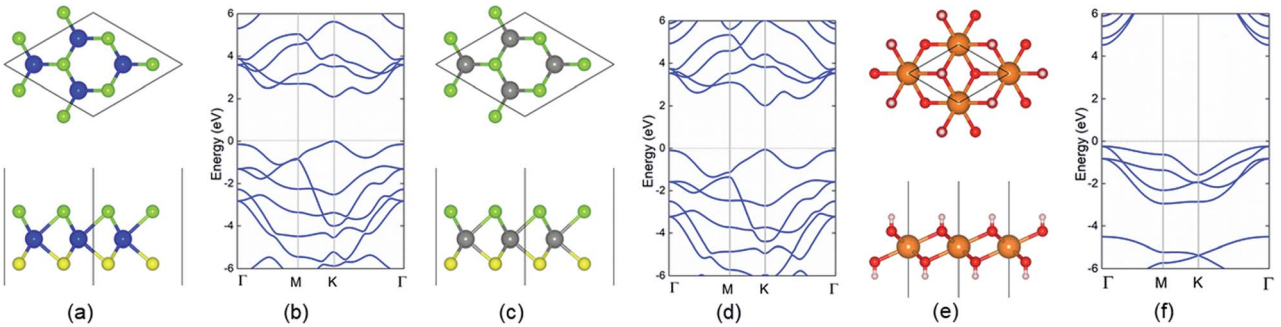

Fig. 1 Schematic of the structures of pristine (a) MoSSe, (c) WSSe and (e) $Mg(OH)_2$ monolayers; the blue, cyan, yellow, grey, orange, red and white spheres represent Mo, Se, S, W, Mg, O and H atoms, respectively. The band structure of pristine (b) MoSSe, (d) WSSe and (f) $Mg(OH)_2$ monolayers obtained by the HSE06 method; the Fermi level is set as 0 shown by dash line.

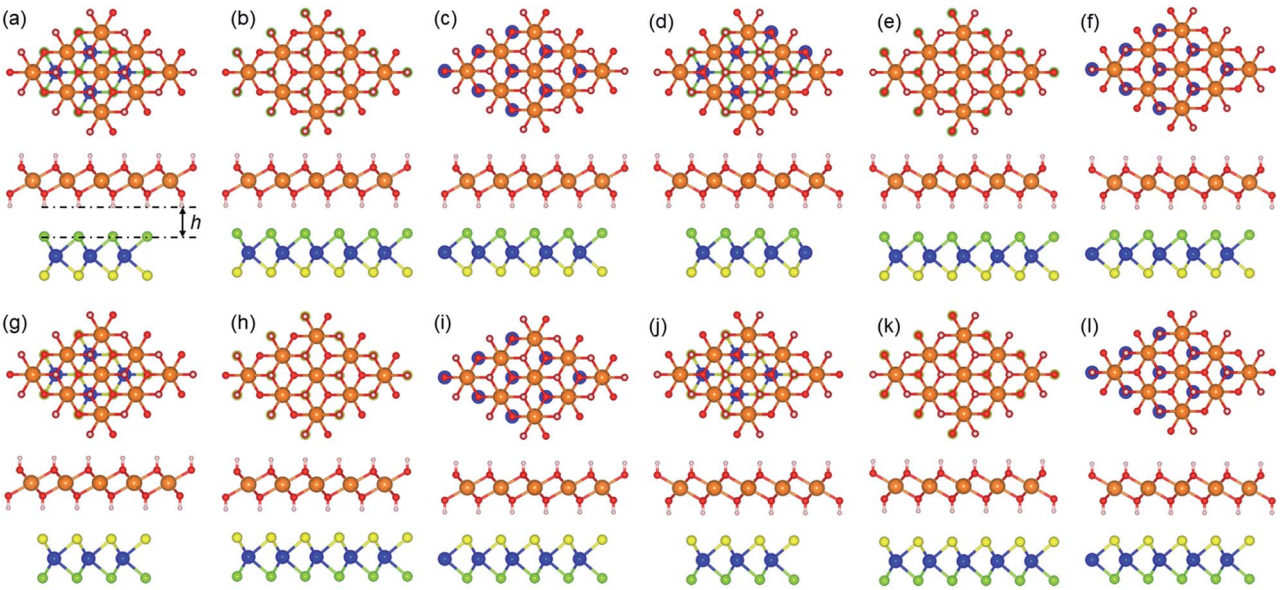

Fig. 2 Top and side views of the $XSSe/Mg(OH)_2$ heterostructures (X = Mo, W) constructed as different stacking styles: (a) S-1, (b) S-2, (c) S-3, (d) S-4, (e) S-5, (f) S-6, (g) S-7, (h) S-8, (i) S-9, (j) S-10, (k) S-11 and (l) S-12.

Table 1 The binding energy (E, meV Å^{-2}), the distance of the interface (h, Å), and bond length (L, Å) of the $XSSe/Mg(OH)_2$ heterostructures constructed by different stacking styles

	$MoSSe/Mg(OH)_2$					$WSSe/Mg(OH)_2$				
	E	h	L_{Mo-S}	L_{Mo-Se}	L_{Mg-O}	E	h	L_{W-S}	L_{W-Se}	L_{Mg-O}
S-1	−76.610	2.54	2.41	2.53	2.12	−78.157	2.55	2.42	2.53	2.13
S-2	−79.617	2.21	2.41	2.53	2.12	−81.506	2.19	2.42	2.54	2.12
S-3	−79.719	2.22	2.41	2.53	2.12	−81.640	2.19	2.42	2.53	2.13
S-4	−79.628	2.22	2.41	2.53	2.13	−81.494	2.19	2.42	2.53	2.12
S-5	−76.588	2.55	2.41	2.53	2.12	−78.124	2.56	2.42	2.53	2.13
S-6	−79.752	2.20	2.41	2.53	2.12	−81.652	2.19	2.42	2.54	2.12
S-7	−75.259	2.47	2.41	2.53	2.12	−57.472	2.15	2.63	2.62	2.07
S-8	−77.134	2.25	2.41	2.53	2.12	−79.157	2.17	2.42	2.54	2.13
S-9	−77.635	2.21	2.41	2.53	2.13	−79.517	2.20	2.42	2.54	2.13
S-10	−77.500	2.18	2.41	2.53	2.13	−79.393	2.17	2.42	2.54	2.13
S-11	−75.248	2.49	2.41	2.53	2.13	−76.910	2.48	2.42	2.54	2.13
S-12	−77.410	2.21	2.41	2.53	2.12	−79.281	2.24	2.42	2.54	2.13

(about 2.76% and 4.02%) for the $MoSSe/Mg(OH)_2$ and $WSSe/Mg(OH)_2$ heterostructures. Besides, the bond length of Mo–S, Mo–Se, W–S, W–Se in the optimized monolayered MoSSe and WSSe were obtained as 2.414, 2.529, 2.428 and 2.542 Å, respectively. Furthermore, the band structures of those layered materials are also demonstrated in Fig. 1. It can be found that MoSSe, WSSe and $Mg(OH)_2$ had direct bandgaps of 2.100, 2.077 and 4.690 eV, respectively, which were in good agreement with other reports.[69,82]

When the heterostructure is formed by XSSe and $Mg(OH)_2$, 12 representative stacking structures should be taken into consideration. Fig. 2 shows these 12 different stacking configurations of $XSSe/Mg(OH)_2$. The most stable stacking style of the $XSSe/Mg(OH)_2$ heterostructure was decided using the binding energy (E), and the E of the $XSSe/Mg(OH)_2$ heterostructure is explained in Table 1, which shows that S-6 is the most stable configuration with the E values of −79.752 and −81.652 meV $Å^{-2}$, respectively. The calculated binding energy of $XSSe/Mg(OH)_2$ demonstrated the vdW forces between the interface of the MoSSe (or WSSe) and $Mg(OH)_2$ monolayers.[83,84] The obtained bond length of Mo–S, Mo–Se, W–S and W–Se of MoSSe and WSSe in their heterostructures, displayed in Table 1, suggested a slight change compared to the pristine MoSSe and WSSe monolayers, which can further prove the weak vdW forces in the $XSSe/Mg(OH)_2$ heterostructure. Besides, the distance of the interface of the $MoSSe/Mg(OH)_2$ and $WSSe/Mg(OH)_2$ vdW heterostructures were obtained to be 2.20 and 2.19 Å, respectively, which were also smaller than that of graphite (3.336 Å).[83] Furthermore, the following investigations of the $XSSe/Mg(OH)_2$ vdW heterostructures are all based on the S-6 stacking configuration.

Then, we also used the AIMD method to further investigate the thermal stability of the $XSSe/Mg(OH)_2$ vdW heterostructures with a Nosé–Hoover heat bath scheme.[85] To consider the constraints of lattice translational, we constructed a $6 \times 6 \times 1$ supercell for the $MoSSe/Mg(OH)_2$ and $WSSe/Mg(OH)_2$ vdW

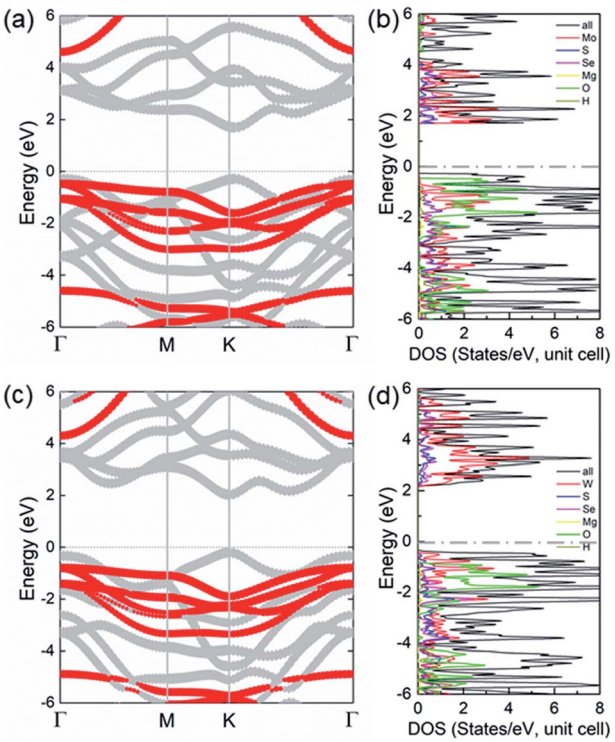

Fig. 4 Projected band structures of the (a) $MoSSe/Mg(OH)_2$ and (c) $WSSe/Mg(OH)_2$ vdW heterostructures; the red and grey marks represent the contributions of the XSSe and $Mg(OH)_2$ layers, the Fermi level is set as 0 shown by dash line. The partial charge densities of the (b) $MoSSe/Mg(OH)_2$ and (d) $WSSe/Mg(OH)_2$ vdW heterostructures.

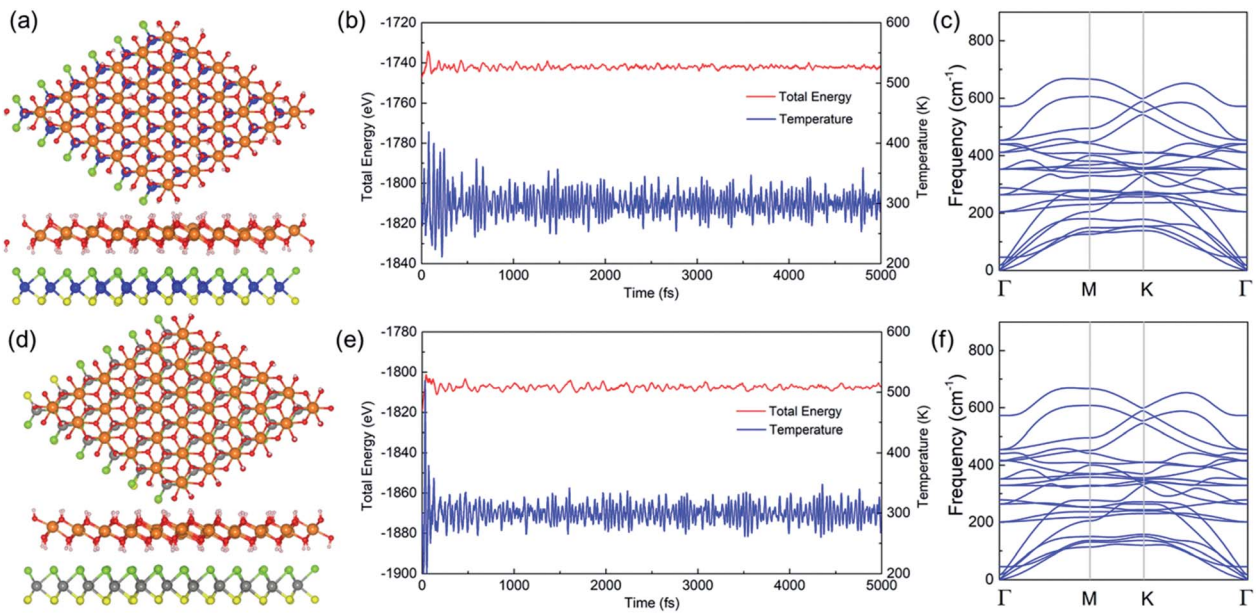

Fig. 3 The snapshot of the (a) $MoSSe/Mg(OH)_2$ and (d) $WSSe/Mg(OH)_2$ vdW heterostructures under the temperature of 300 K after 5 ps; the fluctuations of the temperature and total energy of the (b) $MoSSe/Mg(OH)_2$ and (e) $WSSe/Mg(OH)_2$ system during the AIMD simulation; the phonon dispersions of (c) the $MoSSe/Mg(OH)_2$ and (f) $WSSe/Mg(OH)_2$ vdW heterostructures.

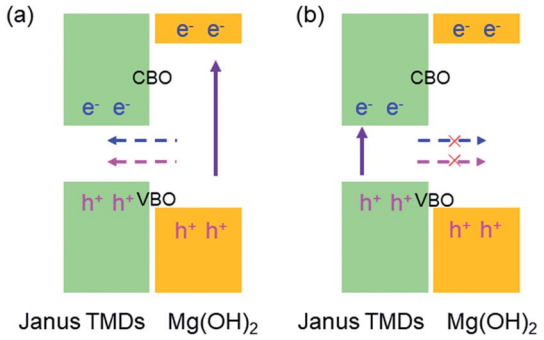

Fig. 5 The band alignment schematic for the migration of free electrons and holes at the interface of the XSSe/$Mg(OH)_2$ vdW heterostructure.

heterostructures in the AIMD simulation, which contained 288 atoms totally. The ambient temperature of the simulation was set as 300 K, and the structures of the MoSSe/$Mg(OH)_2$ and WSSe/$Mg(OH)_2$ vdW heterostructures after relaxation for 5 ps are shown in Fig. 3(a) and (d), respectively. It can be found that the structures of the MoSSe/$Mg(OH)_2$ and WSSe/$Mg(OH)_2$ vdW heterostructures still remained intact after 5 ps under 300 K, revealing the robust thermal stability of the heterostructures. In addition, the change of temperature and total energy during the AIMD calculation of both layered systems are shown in Fig. 3(b) and (e), respectively. The temperature and total energy exhibited a convergence with the simulation step, guaranteeing the reliability of the results. The phonon dispersions were calculated (Fig. 3(c) and (d)) to further evaluate the stability of the MoSSe/$Mg(OH)_2$ and WSSe/$Mg(OH)_2$ vdW heterostructures. It is worth noting that no imaginary frequency existed in their phonon spectra, suggesting a dynamic stability.

The projected band structure of the XSSe/$Mg(OH)_2$ vdW heterostructures shown in Fig. 4 obtained by the HSE06 method. Both MoSSe/$Mg(OH)_2$ and WSSe/$Mg(OH)_2$ vdW heterostructures possess direct bandgaps of 1.996 and 2.233 eV, respectively. The grey and red marks represent the donation of the band from MoSSe (or WSSe) and $Mg(OH)_2$ layers, respectively; thus, the CBM and VBM of the XSSe/$Mg(OH)_2$ vdW heterostructures were contributed by the MoSSe (or WSSe) layer, showing a type-I band structure for the heterostructures. The calculated partial density of states of the XSSe/$Mg(OH)_2$ vdW heterostructures is also shown in Fig. 4(b) and (d), which further explains the type-I band alignment that the CBM and VBM of the MoSSe/$Mg(OH)_2$ and WSSe/$Mg(OH)_2$ vdW heterostructures resulted from Mo and W atoms, respectively.

In the XSSe/$Mg(OH)_2$ vdW heterostructure, the CBM and VBM were both fixed in the layered materials with a narrower bandgap, MoSSe (or WSSe), as shown in Fig. 5. When the electrons in the wide-gap layer, $Mg(OH)_2$, were excited to the CBM, the holes were also induced at the VBM. By the assistance of the conduction band offset (CBO) and valence band offset (VBO), the excited electrons and holes of the $Mg(OH)_2$ layer both

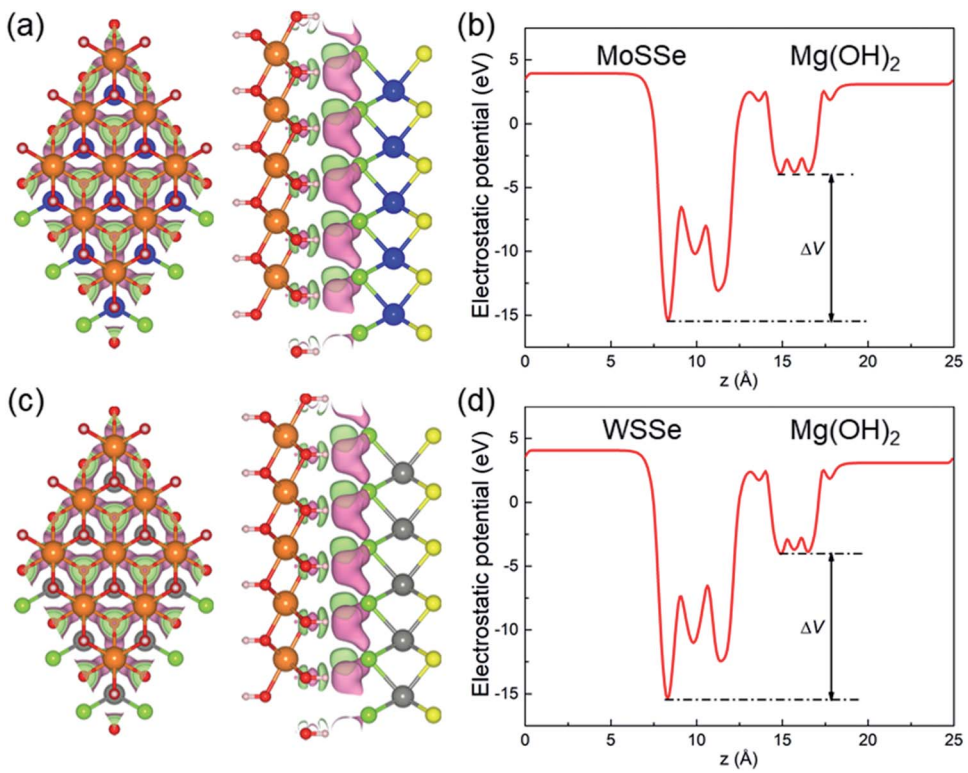

Fig. 6 The isosurfaces of charge density difference of the (a) MoSSe/$Mg(OH)_2$ and (c) WSSe/$Mg(OH)_2$ vdW heterostructures, the obtaining and the losing of electrons are demonstrated by cyan and violet marks, respectively; the isosurface level of charge difference is set as 0.015 |e|; the calculated potential drop across interface of the (b) MoSSe/$Mg(OH)_2$ and (d) WSSe/$Mg(OH)_2$ vdW heterostructures.

migrated to the CBM and VBM of the XSSe layer, respectively, as shown in Fig. 5(a). The CBO and VBO of the MoSSe/$Mg(OH)_2$ (or MoSSe/$Mg(OH)_2$) vdW heterostructure were obtained as 2.937 eV (or 2.260) eV and 0.199 eV (or 0.597 eV), respectively. Besides, the radiative recombination of the electrons and holes was promoted by the quantum confinement in the XSSe layer, suggesting the potential candidate as light-emitting device.[86] Furthermore, the electron–hole pairs excited in the narrow-gap XSSe layer were prevented to transfer to the $Mg(OH)_2$ layer because of the lower energies.[54]

Fig. 6(a) and (c) demonstrate the charge density difference between the interface of the XSSe and $Mg(OH)_2$ layers, which shows that the MoSSe (or WSSe) layer acts as an electron-donor, while $Mg(OH)_2$ layer receives the electrons. Furthermore, the Bader-charge analysis method[87] was employed to quantitatively calculate the electron transfer, and the $Mg(OH)_2$ layer obtained 0.003 (or 0.0042) $|e|$ from the MoSSe (or WSSe) layer in their heterostructure. Such small electron transfers also explain the weak vdW forces between the interface of the XSSe/$Mg(OH)_2$ vdW heterostructures. Besides, after the Janus TMDs contact with the $Mg(OH)_2$ layer and reach an equilibrium, the potential differences between the interface of the heterostructure are addressed, as shown in Fig. 6(b) and (d). There is a potential drop between the interface calculated to be 11.59 and 11.44 eV for MoSSe/$Mg(OH)_2$ and WSSe/$Mg(OH)_2$ vdW heterostructures, respectively, which can also act as an effective driving force to promote the carrier in Fig. 5(a).

The light absorption capacity of the XSSe, $Mg(OH)_2$ and the XSSe/$Mg(OH)_2$ vdW heterostructure were investigated, as shown in Fig. 7. It is obvious that near the wavelength range of visible light (about 380–700 nm) the MoSSe, WSSe and XSSe/$Mg(OH)_2$ vdW heterostructures exhibited an excellent optical absorption spectrum. In detail, the MoSSe/$Mg(OH)_2$ and WSSe/$Mg(OH)_2$ vdW heterostructures possessed pronounced absorption peaks of 5.496×10^5 cm^{-1} and 4.295×10^5 cm^{-1} at 352 nm and 367 nm, respectively. The XSSe/$Mg(OH)_2$ vdW heterostructures displayed the ability to absorb sunlight absorption over a wide range in the visible and NIR regions, which considerably overlap the wavelength range of the solar spectrum. Besides, high absorption peaks appeared in the visible region approximately at the wavelengths of 562 and 495 nm for the MoSSe/$Mg(OH)_2$ and WSSe/$Mg(OH)_2$ vdW heterostructures by 1.432×10^5 cm^{-1} and 1.656×10^5 cm^{-1}, respectively, which were higher than those of other TMD-based heterostructures, such as WS_2/BSe (14.09×104 cm^{-1}),[88] g-GaN/BSe (1.470×10^5 cm^{-1})[89] and g-GaN/BlueP (0.48×10^5 cm^{-1}).[45] The novel optical absorption characteristic of the XSSe/$Mg(OH)_2$ vdW heterostructures also revealed their potential uses as optoelectronic devices.

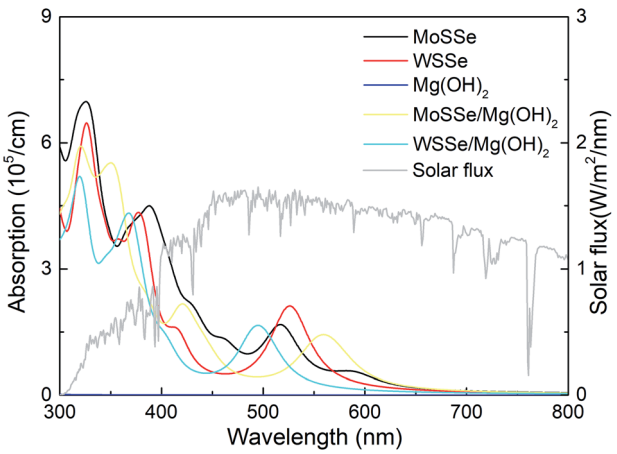

Fig. 7 The optical absorption spectrum of the monolayered XSSe, $Mg(OH)_2$ and XSSe/$Mg(OH)_2$ vdW heterostructures calculated by the HSE06 functional.

4. Conclusions

DFT calculations were explored systematically to study 2D heterostructures based on Janus TMDs and $Mg(OH)_2$. The heterostructures of MoSSe/$Mg(OH)_2$ and WSSe/$Mg(OH)_2$ were formed by vdW forces with thermal and dynamic stability. Importantly, both XSSe/$Mg(OH)_2$ vdW heterostructures possessed a semiconductor performance with direct bandgap values of 1.996 and 2.233 eV, respectively. The band alignment of the XSSe/$Mg(OH)_2$ vdW heterostructure showed a type-I band structure for both heterostructures, which indicates that they are desirable candidates for light-emitting devices. Besides, the charge density difference analysis demonstrated that the MoSSe and WSSe layers donated 0.003 and 0.0042 $|e|$ to the $Mg(OH)_2$ layer in their heterostructures, respectively. Furthermore, both heterostructure had fantastic visible light absorptivity. The work provides a theoretical guidance to design new heterostructures based on Janus TMD materials for future nano-devices.

Conflicts of interest

There are no conflicts to declare.

Acknowledgements

This work was supported by the project of the Development and application of key equipment for intelligent spraying technology of automobile parts (00520088), the Development and application of complete set of intelligent testing equipment for automobile lamp (00520188) and the Open Fund Project of Maanshan Engineering Technology Research Center of Advanced Design for Automotive Stamping Dies (QMSG202105).

References

1 A. K. Geim and K. S. Novoselov, The rise of graphene, *Nat. Mater.*, 2007, **6**, 183–191.
2 M. D. Stoller, S. Park, Y. Zhu, J. An and R. S. Ruoff, Graphene-based ultracapacitors, *Nano Lett.*, 2008, **8**, 3498–3502.
3 J. Zhou, J. Lin, X. Huang, Y. Zhou, Y. Chen, J. Xia, H. Wang, Y. Xie, H. Yu, J. Lei, D. Wu, F. Liu, Q. Fu, Q. Zeng, C. H. Hsu, C. Yang, L. Lu, T. Yu, Z. Shen, H. Lin, B. I. Yakobson, Q. Liu, K. Suenaga, G. Liu and Z. Liu, A library of atomically thin metal chalcogenides, *Nature*, 2018, **556**, 355–359.

4 H. Zhang, M. Chhowalla and Z. Liu, 2D nanomaterials: graphene and transition metal dichalcogenides, *Chem. Soc. Rev.*, 2018, **47**, 3015–3017.
5 S. Zhou, Y. Guo and J. Zhao, Enhanced thermoelectric properties of graphene oxide patterned by nanoroads, *Phys. Chem. Chem. Phys.*, 2016, **18**, 10607–10615.
6 L. Liu, X. Li, Z. Liu, S. Dai, X. Huang and J. Zhao, Tunable bending modulus and bending limit of oxidized graphene, *Nanoscale*, 2020, **12**, 1623–1628.
7 M. Sun, Q. Ren, Y. Zhao, J.-P. Chou, J. Yu and W. Tang, Electronic and magnetic properties of 4d series transition metal substituted graphene: A first-principles study, *Carbon*, 2017, **120**, 265–273.
8 M. Sun, J. P. Chou, J. Yu and W. Tang, Electronic properties of blue phosphorene/graphene and blue phosphorene/graphene-like gallium nitride heterostructures, *Phys. Chem. Chem. Phys.*, 2017, **19**, 17324–17330.
9 M. Sun, J. P. Chou, Y. Zhao, J. Yu and W. Tang, Weak C-HF-C hydrogen bonds make a big difference in graphane/fluorographane and fluorographene/fluorographane bilayers, *Phys. Chem. Chem. Phys.*, 2017, **19**, 28127–28132.
10 R. Li, Y. Cheng and W. Huang, Recent Progress of Janus 2D Transition Metal Chalcogenides: From Theory to Experiments, *Small*, 2018, **14**, e1802091.
11 S. Z. Butler, S. M. Hollen, L. Cao, Y. Cui, J. A. Gupta, H. R. Gutiérrez, T. F. Heinz, S. S. Hong, J. Huang and A. F. Ismach, Progress, challenges, and opportunities in two-dimensional materials beyond graphene, *ACS Nano*, 2013, **7**, 2898–2926.
12 Q. Liu, J. Xing, Z. Jiang, X. Jiang, Y. Wang and J. Zhao, 2D tetragonal transition-metal phosphides: an ideal platform to screen metal shrouded crystals for multifunctional applications, *Nanoscale*, 2020, **12**, 6776–6784.
13 J. Jiang, F. Sun, S. Zhou, W. Hu, H. Zhang, J. Dong, Z. Jiang, J. Zhao, J. Li and W. Yan, Atomic-level insight into super-efficient electrocatalytic oxygen evolution on iron and vanadium co-doped nickel (oxy) hydroxide, *Nat. Commun.*, 2018, **9**, 1–12.
14 Y. Guo, L. Ma, K. Mao, M. Ju, Y. Bai, J. Zhao and X. C. Zeng, Eighteen functional monolayer metal oxides: wide bandgap semiconductors with superior oxidation resistance and ultrahigh carrier mobility, *Nanoscale Horiz.*, 2019, **4**, 592–600.
15 S. Zhou, N. Liu and J. Zhao, Phosphorus quantum dots as visible-light photocatalyst for water splitting, *Comput. Mater. Sci.*, 2017, **130**, 56–63.
16 Y. Gao, D. Sun, X. Jiang and J. Zhao, Point defects in group III nitrides: A comparative first-principles study, *J. Appl. Phys.*, 2019, **125**, 215705.
17 S. Zhou and J. Zhao, Two-dimensional B–C–O alloys: a promising class of 2D materials for electronic devices, *Nanoscale*, 2016, **8**, 8910–8918.
18 Y. Li, Q. Cui, F. Ceballos, S. D. Lane, Z. Qi and H. Zhao, Ultrafast Interlayer Electron Transfer in Incommensurate Transition Metal Dichalcogenide Homobilayers, *Nano Lett.*, 2017, **17**, 6661–6666.
19 Y. Cai, J. Lan, G. Zhang and Y.-W. Zhang, Lattice vibrational modes and phonon thermal conductivity of monolayer MoS_2, *Phys. Rev. B*, 2014, **89**, 035438.
20 K. Ren, M. Sun, Y. Luo, S. Wang, J. Yu and W. Tang, First-principle study of electronic and optical properties of two-dimensional materials-based heterostructures based on transition metal dichalcogenides and boron phosphide, *Appl. Surf. Sci.*, 2019, **476**, 70–75.
21 D. Y. Qiu, H. Felipe and S. G. Louie, Optical spectrum of MoS_2: many-body effects and diversity of exciton states, *Phys. Rev. Lett.*, 2013, **111**, 216805.
22 K. Chen, D. Kiriya, M. Hettick, M. Tosun, T.-J. Ha, S. R. Madhvapathy, S. Desai, A. Sachid and A. Javey, Air stable n-doping of WSe2 by silicon nitride thin films with tunable fixed charge density, *APL Mater.*, 2014, **2**, 092504.
23 D. Wickramaratne, F. Zahid and R. K. Lake, Electronic and thermoelectric properties of few-layer transition metal dichalcogenides, *J. Chem. Phys.*, 2014, **140**, 124710.
24 B. Radisavljevic, A. Radenovic, J. Brivio, V. Giacometti and A. Kis, Single-layer MoS_2 transistors, *Nat. Nanotechnol.*, 2011, **6**, 147–150.
25 S. Zhou and J. Zhao, Electronic structures of germanene on MoS_2: effect of substrate and molecular adsorption, *J. Phys. Chem. C*, 2016, **120**, 21691–21698.
26 S. Zhou, N. Liu, Z. Wang and J. Zhao, Nitrogen-doped graphene on transition metal substrates as efficient bifunctional catalysts for oxygen reduction and oxygen evolution reactions, *ACS Appl. Mater. Interfaces*, 2017, **9**, 22578–22587.
27 Y. Luo, S. Wang, H. Shu, J.-P. Chou, K. Ren, J. Yu and M. Sun, A MoSSe/blue phosphorene vdw heterostructure with energy conversion efficiency of 19.9% for photocatalytic water splitting, *Semicond. Sci. Technol.*, 2020, **35**, 125008.
28 M. Sun, J.-P. Chou, A. Hu and U. Schwingenschlögl, Point Defects in Blue Phosphorene, *Chem. Mater.*, 2019, **31**, 8129–8135.
29 J. Li, Z. Huang, W. Ke, J. Yu, K. Ren and Z. Dong, High solar-to-hydrogen efficiency in Arsenene/GaX (X = S, Se) van der Waals heterostructure for photocatalytic water splitting, *J. Alloys Compd.*, 2021, 866.
30 M. Sun, J.-P. Chou, J. Yu and W. Tang, Effects of structural imperfection on the electronic properties of graphene/WSe_2 heterostructures, *J. Mater. Chem. C*, 2017, **5**, 10383–10390.
31 S. Wang, C. Ren, H. Tian, J. Yu and M. Sun, MoS_2/ZnO van der Waals heterostructure as a high-efficiency water splitting photocatalyst: a first-principles study, *Phys. Chem. Chem. Phys.*, 2018, **20**, 13394–13399.
32 M. Sun and U. Schwingenschlögl, B_2P_6: A Two-Dimensional Anisotropic Janus Material with Potential in Photocatalytic Water Splitting and Metal-Ion Batteries, *Chem. Mater.*, 2020, **32**, 4795–4800.
33 M. Sun, Y. Yan and U. Schwingenschlögl, Beryllene: A Promising Anode Material for Na-and K-Ion Batteries with Ultrafast Charge/Discharge and High Specific Capacity, *J. Phys. Chem. Lett.*, 2020, **11**, 9051–9056.

34 M. Sun and U. Schwingenschlögl, *Structure Prototype Outperforming MXenes in Stability and Performance in Metal-Ion Batteries: A High Throughput Study*, Advanced Energy Materials, 2021.
35 M. Sun and U. Schwingenschlögl, Unique Omnidirectional Negative Poisson's Ratio in δ-Phase Carbon Monochalcogenides, *J. Phys. Chem. C*, 2021, **125**, 4133–4138.
36 M. Sun and U. Schwingenschlögl, δ-CS: A Direct-Band-Gap Semiconductor Combining Auxeticity, Ferroelasticity, and Potential for High-Efficiency Solar Cells, *Phys. Rev. Appl.*, 2020, **14**, 044015.
37 H. Wang, X. Li, P. Li and J. Yang, δ-Phosphorene: a two dimensional material with a highly negative Poisson's ratio, *Nanoscale*, 2017, **9**, 850–855.
38 H. Zhang, Y. Li, J. Hou, A. Du and Z. Chen, Dirac State in the FeB_2 Monolayer with Graphene-Like Boron Sheet, *Nano Lett.*, 2016, **16**, 6124–6129.
39 T. Yu, Z. Zhao, L. Liu, S. Zhang, H. Xu and G. Yang, TiC_3 Monolayer with High Specific Capacity for Sodium-Ion Batteries, *J. Am. Chem. Soc.*, 2018, **140**, 5962–5968.
40 B. Wang, Q. Wu, Y. Zhang, Y. Guo, X. Zhang, Q. Zhou, S. Dong and J. Wang, High Curie-temperature intrinsic ferromagnetism and hole doping-induced half-metallicity in two-dimensional scandium chlorine monolayers, *Nanoscale Horiz.*, 2018, **3**, 551–555.
41 K. S. Novoselov, A. Mishchenko, A. Carvalho and A. H. Castro Neto, 2D materials and van der Waals heterostructures, *Science*, 2016, **353**, aac9439.
42 D. L. Duong, S. J. Yun and Y. H. Lee, van der Waals Layered Materials: Opportunities and Challenges, *ACS Nano*, 2017, **11**, 11803–11830.
43 K. Ren, R. Zheng, P. Xu, D. Cheng, W. Huo, J. Yu, Z. Zhang and Q. Sun, Electronic and Optical Properties of Atomic-Scale Heterostructure Based on MXene and MN (M = Al, Ga): A DFT Investigation, *Nanomaterials*, 2021, **11**(9), 2236.
44 K. Ren, K. Wang, Y. Cheng, W. Tang and G. Zhang, Two-dimensional heterostructures for photocatalytic water splitting: a review of recent progress, *Nano Futures*, 2020, **4**, 032006.
45 K. Ren, S. Wang, Y. Luo, Y. Xu, M. Sun, J. Yu and W. Tang, Strain-enhanced properties of van der Waals heterostructure based on blue phosphorus and g-GaN as a visible-light-driven photocatalyst for water splitting, *RSC Adv.*, 2019, **9**, 4816–4823.
46 Y. Yan, Z. Zeng, M. Huang and P. Chen, Van der waals heterojunctions for catalysis, *Mater. Today Adv.*, 2020, **6**, 100059.
47 K. Ren, W. Tang, M. Sun, Y. Cai, Y. Cheng and G. Zhang, A direct Z-scheme PtS_2/arsenene van der Waals heterostructure with high photocatalytic water splitting efficiency, *Nanoscale*, 2020, **12**, 17281–17289.
48 Y. Liu, N. O. Weiss, X. Duan, H.-C. Cheng, Y. Huang and X. Duan, Van der Waals heterostructures and devices, *Nat. Rev. Mater.*, 2016, **1**, 16042.
49 R. Kumar, D. Das and A. K. Singh, C_2N/WS_2 van der Waals type-II heterostructure as a promising water splitting photocatalyst, *J. Catal.*, 2018, **359**, 143–150.
50 R. Zhang, L. Zhang, Q. Zheng, P. Gao, J. Zhao and J. Yang, Direct Z-scheme water splitting photocatalyst based on two-dimensional Van Der Waals heterostructures, *J. Phys. Chem. Lett.*, 2018, **9**, 5419–5424.
51 R. Shi, F. Liu, Z. Wang, Y. Weng and Y. Chen, Black/red phosphorus quantum dots for photocatalytic water splitting: from a type I heterostructure to a Z-scheme system, *Chem. Commun.*, 2019, **55**, 12531–12534.
52 T. Yamaoka, H. E. Lim, S. Koirala, X. Wang, K. Shinokita, M. Maruyama, S. Okada, Y. Miyauchi and K. Matsuda, Efficient Photocarrier Transfer and Effective Photoluminescence Enhancement in Type I Monolayer $MoTe_2$/WSe_2 Heterostructure, *Adv. Funct. Mater.*, 2018, **28**, 1801021.
53 W. Zheng, B. Zheng, Y. Jiang, C. Yan, S. Chen, Y. Liu, X. Sun, C. Zhu, Z. Qi, T. Yang, W. Huang, P. Fan, F. Jiang, X. Wang, X. Zhuang, D. Li, Z. Li, W. Xie, W. Ji, X. Wang and A. Pan, Probing and Manipulating Carrier Interlayer Diffusion in van der Waals Multilayer by Constructing Type-I Heterostructure, *Nano Lett.*, 2019, **19**, 7217–7225.
54 M. Z. Bellus, M. Li, S. D. Lane, F. Ceballos, Q. Cui, X. C. Zeng and H. Zhao, Type-I van der Waals heterostructure formed by MoS2 and ReS2 monolayers, *Nanoscale Horiz.*, 2017, **2**, 31–36.
55 M. Virgilio and G. Grosso, Type-I alignment and direct fundamental gap in SiGe based heterostructures, *J. Phys.: Condens. Matter*, 2006, **18**, 1021–1031.
56 D. Dorfs, T. Franzl, R. Osovsky, M. Brumer, E. Lifshitz, T. A. Klar and A. Eychmuller, Type-I and type-II nanoscale heterostructures based on CdTe nanocrystals: a comparative study, *Small*, 2008, **4**, 1148–1152.
57 T.-N. Do, M. Idrees, N. T. T. Binh, H. V. Phuc, N. N. Hieu, L. T. Hoa, B. Amin and H. Van, Type-I band alignment of BX–ZnO (X = As, P) van der Waals heterostructures as high-efficiency water splitting photocatalysts: a first-principles study, *RSC Adv.*, 2020, **10**, 44545–44550.
58 L. Ju, M. Bie, X. Zhang, X. Chen and L. Kou, Two-dimensional Janus van der Waals heterojunctions: A review of recent research progresses, *Front. Phys.*, 2021, **16**, 1–16.
59 J. Zhang, S. Jia, I. Kholmanov, L. Dong, D. Er, W. Chen, H. Guo, Z. Jin, V. B. Shenoy, L. Shi and J. Lou, Janus Monolayer Transition-Metal Dichalcogenides, *ACS Nano*, 2017, **11**, 8192–8198.
60 A. Y. Lu, H. Zhu, J. Xiao, C. P. Chuu, Y. Han, M. H. Chiu, C. C. Cheng, C. W. Yang, K. H. Wei, Y. Yang, Y. Wang, D. Sokaras, D. Nordlund, P. Yang, D. A. Muller, M. Y. Chou, X. Zhang and L. J. Li, Janus monolayers of transition metal dichalcogenides, *Nat. Nanotechnol.*, 2017, **12**, 744–749.
61 J. Wang, H. Shu, T. Zhao, P. Liang, N. Wang, D. Cao and X. Chen, Intriguing electronic and optical properties of two-dimensional Janus transition metal dichalcogenides, *Phys. Chem. Chem. Phys.*, 2018, **20**, 18571–18578.
62 W.-J. Yin, X.-L. Zeng, B. Wen, Q.-X. Ge, Y. Xu, G. Teobaldi and L.-M. Liu, The unique carrier mobility of Janus MoSSe/GaN heterostructures, *Front. Phys.*, 2021, **16**, 1–9.

63 P. Zhao, Y. Liang, Y. Ma, B. Huang and Y. Dai, Janus Chromium Dichalcogenide Monolayers with Low Carrier Recombination for Photocatalytic Overall Water-Splitting under Infrared Light, *J. Phys. Chem. C*, 2019, **123**, 4186–4192.

64 X. Ma, X. Wu, H. Wang and Y. Wang, A Janus MoSSe monolayer: a potential wide solar-spectrum water-splitting photocatalyst with a low carrier recombination rate, *J. Mater. Chem. A*, 2018, **6**, 2295–2301.

65 D. Er, H. Ye, N. C. Frey, H. Kumar, J. Lou and V. B. Shenoy, Prediction of Enhanced Catalytic Activity for Hydrogen Evolution Reaction in Janus Transition Metal Dichalcogenides, *Nano Lett.*, 2018, **18**, 3943–3949.

66 C. Xia, W. Xiong, J. Du, T. Wang, Y. Peng and J. Li, Universality of electronic characteristics and photocatalyst applications in the two-dimensional Janus transition metal dichalcogenides, *Phys. Rev. B*, 2018, **98**, 165424.

67 A. Suslu, K. Wu, H. Sahin, B. Chen, S. Yang, H. Cai, T. Aoki, S. Horzum, J. Kang, F. M. Peeters and S. Tongay, Unusual dimensionality effects and surface charge density in 2D $Mg(OH)_2$, *Sci. Rep.*, 2016, **6**, 20525.

68 K. Ren, J. Yu and W. Tang, First-principles study of two-dimensional van der Waals heterostructure based on ZnO and $Mg(OH)_2$: A potential photocatalyst for water splitting, *Phys. A*, 2019, 125916.

69 K. Ren, J. Yu and W. Tang, A two-dimensional vertical van der Waals heterostructure based on g-GaN and $Mg(OH)_2$ used as a promising photocatalyst for water splitting: A first-principles calculation, *J. Appl. Phys.*, 2019, **126**, 065701.

70 F. Li, W. Wei, P. Zhao, B. Huang and Y. Dai, Electronic and Optical Properties of Pristine and Vertical and Lateral Heterostructures of Janus MoSSe and WSSe, *J. Phys. Chem. Lett.*, 2017, **8**, 5959–5965.

71 T. Jing, D. Liang, J. Hao, M. Deng and S. Cai, Interface Schottky barrier in Hf_2NT_2/MSSe (T = F, O, OH; M = Mo, W) heterostructures, *Phys. Chem. Chem. Phys.*, 2019, 5394–5401.

72 Y. Liang, J. Li, H. Jin, B. Huang and Y. Dai, Photoexcitation Dynamics in Janus-MoSSe/WSe_2 Heterobilayers: Ab Initio Time-Domain Study, *J. Phys. Chem. Lett.*, 2018, **9**, 2797–2802.

73 Y. Li, J. Wang, B. Zhou, F. Wang, Y. Miao, J. Wei, B. Zhang and K. Zhang, Tunable interlayer coupling and Schottky barrier in graphene and Janus MoSSe heterostructures by applying an external field, *Phys. Chem. Chem. Phys.*, 2018, **20**, 24109–24116.

74 S. Grimme, J. Antony, S. Ehrlich and H. Krieg, A consistent and accurate ab initio parametrization of density functional dispersion correction (DFT-D) for the 94 elements H-Pu, *J. Chem. Phys.*, 2010, **132**, 154104.

75 G. Kresse and J. Furthmüller, Efficiency of ab-initio total energy calculations for metals and semiconductors using a plane-wave basis set, *Comput. Mater. Sci.*, 1996, **6**, 15–50.

76 G. Kresse and J. Furthmüller, Efficient iterative schemes for ab initio total-energy calculations using a plane-wave basis set, *Phys. Rev. B*, 1996, **54**, 11169.

77 G. Kresse and D. Joubert, From ultrasoft pseudopotentials to the projector augmented-wave method, *Phys. Rev. B*, 1999, **59**, 1758.

78 J. Heyd, G. E. Scuseria and M. Ernzerhof, Hybrid functionals based on a screened Coulomb potential, *J. Chem. Phys.*, 2003, **118**, 8207–8215.

79 S. Grimme, Semiempirical GGA-type density functional constructed with a long-range dispersion correction, *J. Comput. Chem.*, 2006, **27**, 1787–1799.

80 A. Togo and I. J. S. M. Tanaka, First principles phonon calculations in materials science, *Scr. Mater.*, 2015, **108**, 1–5.

81 A. Togo, F. Oba and I. J. P. R. B. Tanaka, First-principles calculations of the ferroelastic transition between rutile-type and $CaCl_2$-type SiO_2 at high pressures, *Phys. Rev. B*, 2008, **78**, 134106.

82 K. Ren, S. Wang, Y. Luo, J.-P. Chou, J. Yu, W. Tang and M. Sun, High-efficiency photocatalyst for water splitting: a Janus MoSSe/XN (X = Ga, Al) van der Waals heterostructure, *J. Phys. D: Appl. Phys.*, 2020, **53**, 185504.

83 X. Chen, F. Tian, C. Persson, W. Duan and N. X. Chen, Interlayer interactions in graphites, *Sci. Rep.*, 2013, **3**, 3046.

84 T. Bjorkman, A. Gulans, A. V. Krasheninnikov and R. M. Nieminen, van der Waals bonding in layered compounds from advanced density-functional first-principles calculations, *Phys. Rev. Lett.*, 2012, **108**, 235502.

85 S. Nosé, A unified formulation of the constant temperature molecular dynamics methods, *J. Chem. Phys.*, 1984, **81**, 511–519.

86 Z. Lu, D. Lockwood and J.-M. Baribeau, Quantum confinement and light emission in SiO_2/Si superlattices, *Nature*, 1995, **378**, 258–260.

87 W. Tang, E. Sanville and G. Henkelman, A grid-based Bader analysis algorithm without lattice bias, *J. Phys.: Condens. Matter*, 2009, **21**, 084204.

88 Y. Luo, K. Ren, S. Wang, J.-P. Chou, J. Yu, Z. Sun and M. Sun, First-Principles Study on Transition-Metal Dichalcogenide/BSe van der Waals Heterostructures: A Promising Water-Splitting Photocatalyst, *J. Phys. Chem. C*, 2019, **123**, 22742–22751.

89 K. Ren, Y. Luo, S. Wang, J.-P. Chou, J. Yu, W. Tang and M. Sun, A van der Waals Heterostructure Based on Graphene-like Gallium Nitride and Boron Selenide: A High-Efficiency Photocatalyst for Water Splitting, *ACS Omega*, 2019, **4**, 21689–21697.